Biointerface Research in Applied Chemistry
Platinum Open Access Journal (ISSN: 2069-5837)

Article
Volume 12, Issue 4, 2022, 5021 - 5030
https://doi.org/10.33263/BRIAC124.50215030

Modified Structural and Magnetic Properties of Ni-Mn-Zn Ferrite Nanoparticles Doped with Ce^{3+}Ions

Vikram More [1], **Supriya Kadam** [2], **Satish Shelke** [3], **Pravin Gaikwad** [4], **Ramkrishna Kadam** [5,*], **Suresh Alone** [1]

[1] Department of Physics, RajarshiShahu College, Pathri, Dist. Aurangabad, (M.S.) India; vikrammore2292@gmail.com (V.M.);
[2] Department of Physics, Jawahar College, Anadur, Dist. Osmanabad, (M.S.) India; supriya1551988@gmail.com (S.R.K.);
[3] Department of Physics, S.M.P. College, Murum Dist. Osmanabad (M.S.) India; drsbshelke@gmail.com (S.B.S.);
[4] Department of Physics, Shivaji College, Omerga, Dist. Osmanabd (M.S.) India; drpkgaikwad@gmail.com (P.K.G.);
[5] Department of Physics, ShrikrishnaMahavidyalaya, Gunjoti, Dist. Osmanabad (M.S.) India;ram111612@yahoo.co.in (R.H.K.);
* Correspondence: ram111612@yahoo.co.in (R.H.K.);

Scopus Author ID 36018446200

Received: 28.07.2021; Revised: 20.09.2021; Accepted: 24.09.2021; Published: 17.10.2021

Abstract: Polycrystalline Ni-Mn-Zn nano-ferrites doped by the fractional amount of Ce^{3+} ions were fabricated using the sol-gel method. Characterizations of the as-prepared samples were performed by using X-ray diffraction (XRD), scanning electron microscopy (SEM), energy dispersive X-ray analysis (EDAX), vibrating sample magnetometer (VSM), and dielectric measurements. Rietveld refined XRD patterns revealed the single-phase cubic spinel structure of the samples corresponds to the space group Fd-3m. Minor shifting of peak positions towards lower diffraction angles increases lattice parameter from 8.4105 to 8.4193 Å with the addition of Ce^{3+} ions. , The surface morphology and homogeneity of the samples were investigated by using SEM and EDAX spectra. Grain size obtained from SEM analysis is found in the range 29 nm to 33 nm with negligible agglomeration. Analysis of EDAX spectra confirms the stoichiometric proportion of the constituents. Substitution of Ce^{3+} ions shows typical ferromagnetic curves with enhanced saturation magnetization and magneton number from 54 to 63 emu/gm and 2.71 to 3.09 μ_B respectively. Dielectric measurements of the entire samples show the typical behavior of spinel ferrite. The results predict that the samples are best suitable for high-frequency region applications.

Keywords: Rietveld refinement; grain size; saturation magnetization; dielectric properties.

1. Introduction

Since the last several years' ferrites with spinel structures have been extensively used in various technological applications such as microwave devices, recording media, high-frequency transformer cores, intelligent transformer cores, magnetic fluids, and medical diagnostics [1-6]; presently, these nano-scale materials have been synthesized in large amounts for their improved properties [7-10]. In particular, the high electrical resistivity of soft ferrites makes them suitable for high-frequency applications due to low losses of eddy currents in AC fields [11]. The conduction mechanism in these materials depends upon the synthesis routs, nature and percentage of impurity added, and sintering conditions which have been the subject of continuous investigation. When the particle size approaches its critical size, below which each particle behaves as a single domain and hence electrical and magnetic properties are greatly influenced at nano-scale dimensions [12]. Modern data storage devices require better control of the morphology and size of the particles.

Among the class of soft ferrites, mixed Mn-Zn and Ni-Zn ferrites gained more attention due to their high electrical resistivity (~ 10^7 ohm), low-cost synthesis, and dielectric loss, very high mechanical strength, and chemical stability [13, 14]. It becomes an interesting subject to substituting a small amount of rare-earth (RE) ions in mixed Ni-Mn-Zn ferrites. Literature reports suggest that the substation of the fractional amount of RE ions in spinel lattices induces a significant change in electrical and magnetic properties [15-18]. The strong spin-orbit coupling of angular momentum and 4f unpaired electrons observed in RE ions introduces RE-Fe interactions, which significantly influences the magnetic behavior of spinel ferrites. Several researchers have made attempts to investigate the RE substitution effect on the physicochemical properties of spinel ferrites. M. R. Narsabadi *et al*. have investigated that the Ce^{3+} doped copper ferrite nanoparticles can be used as efficient photocatalysts for the photocatalytic degradation of harmful organic dye. [19]. M. H. Abdellatif *et al*. have studied the effect of RE ions (La, Ce, Sm, Gd, and Dy) on the vibrational spectra of Mn-Cr spinel ferrites [20]. A. B. Gadkari *et al*. have reported that the Y^{3+} ions doped in Mg-Cd ferrites occupy the octahedral – B site [21]. S. K. Gurav *et al*. have studied the effect of Zr^{4+}-Zn^{2+} co-substitution on lithium ferrites' structural and magnetic properties [22]. Recently, the Ce^{3+} substitution effect on spinel ferrites' magnetic and electrical properties has been reported [23-25]. To the best of our knowledge, no reports are available on the Ce^{3+} substituted Ni-Mn-Zn mixed ferrites. By keeping the above facts in mind, we have aimed to synthesize and characterize the Ce^{3+} doped Ni-Mn-Zn ferrite nanoparticles.

Numerous synthesis methods have been developed to fabricate pure and doped ferrites, even at low temperatures and low cost. Sol-gel synthesis is one of the best approaches to producing ferrite nanoparticles at low temperatures with better homogeneity and high yield [26, 27]. In the present work, we have adopted the sol-gel synthesis approach to fabricate $Ni_{0.35}Mn_{0.35}Zn_{0.3}Fe_{2-x}Ce_xO_4$ ferrite nanoparticles. The newly prepared samples were characterized by X-ray diffraction (XRD), scanning electron microscopy (SEM), energy dispersive X-ray analysis spectra (EDAX), vibrating sample magnetometer (VSM), and dielectric properties.

2. Materials and Methods

Polycrystalline nanocrystals of $Ni_{0.35}Mn_{0.35}Zn_{0.3}Fe_{2-x}Ce_xO_4$ (x = 0.0, 0.025, 0.050, 0.075 and 0.1) were fabricated by using sol-gel auto-ignition route. Ultra-pure (>98.5%) A. R. grade metal nitrates of constituent elements $Ni(NO_3)_2{\cdot}H_{12}O_6$, $Mn(NO_3)_2{\cdot}H_{12}O_6$, $Zn(NO_3)_2{\cdot}H_{12}O_6$, $Fe(NO_3)_3{\cdot}H_{18}O_9$ and $Ce(NO_3)_3{\cdot}\ H_{18}O_9$ (Sigma Aldrich, USA) were taken as starting materials. All the starting materials were dissolved with their stoichiometric proportion in a sufficient amount of double-distilled deionized water. The mixed solution was kept on a hot plate with a magnetic stirrer for continuous stirring at a constant temperature of 90 ^{0}C. Chelating agent citric acid was mixed in the nitrate solution with the stoichiometric ratio of 1:3 of metal nitrate to citrate. The pH of the solution was kept constant at 7 by slowly adding the liquid ammonia to the solution. Continuous stirring at constant pH and temperature for 2 to 3 hours converts the solution into a viscous gel. After half an hour, the dark brown gel was burnt by self – ignition process and converted into brown ash. Final powders were obtained after final sintering at 900^0C for 6 hours.

Powder X-ray diffraction (Philips, Model 3710) patterns were recorded at room temperature within the 2θ range of 20^0 to 70^0 by using Cu-$K_\alpha$radiations having the incident wavelength λ = 1.5406 Å. The microstructure and surface morphology of the samples were understood using transmission electron microscopy (JEOL JEM 2100). Magnetic characterization was carried out by applying the magnetic field up to 15KOe by employing a vibrating sample magnetometer. Disc-shaped samples with silver paste were used to understand the dielectric behavior of the samples within the frequency range 50Hz to 50MHz by using Hioki HiTESTER 3532-50.

3. Results and Discussion

Sharp Bragg's lines are observed in the Rietveld refined XRD patterns (Figure 1) of $Ni_{0.35}Mn_{0.35}Zn_{0.3}Fe_{2-x}Ce_xO_4$ which are indexed well for the intensity planes (220), (311), (222), (400), (422), (333), and (440). All the indexed planes representing the cubic spinel structure of the samples with space group Fd-3m and indexed to the zinc ferrite, confirmed by standard COD card No. 96-900-6895 [28]. No traces of secondary phases are observed in the XRD patterns, confirming the samples' phase purity. Close observation of the most intensive peak (311) (Figure 1(F)) shows that the addition of Ce^{3+} ions in Ni-Mn-Zn ferrites decreases peak intensity, while peak positions shifted slightly towards lower diffraction angles. Lattice parameter 'a' and the data obtained from Rietveld refinement of X-ray diffraction patterns by FullProf software are given in Table 1. The refinement has been continued until the value of goodness factor (χ^2) reaches between 1 and 2. The obtained values of the lattice parameter as a function of Ce^{3+} addition lie in the range of 8.4105 Å to 8.4193 Å. The increase in lattice parameter is closely related to the shifting of peak positions towards lower diffraction angles. The reason behind this is the replacement of Fe^{3+} ions having lower ionic radii (0.069 nm) by Ce^{3+} ions having higher ionic radii (0.115 nm).

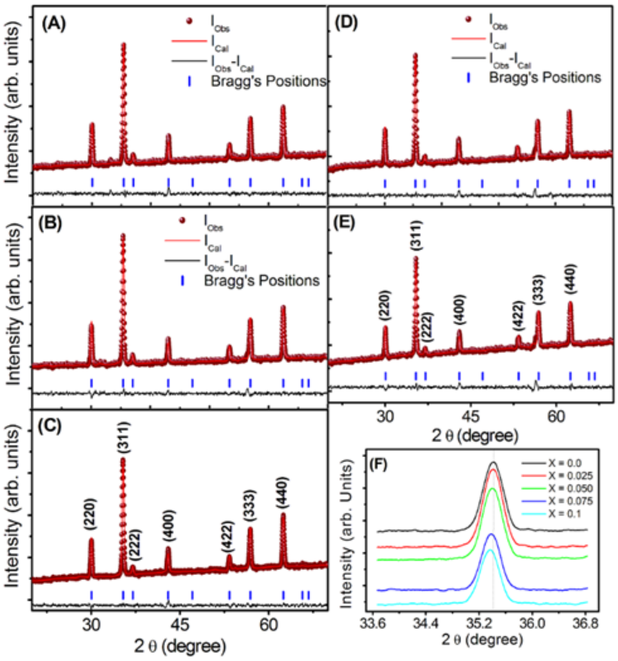

Figure 1. Rietveld refined XRD patterns of $Ni_{0.35}Mn_{0.35}Zn_{0.3}Fe_{2-x}Ce_xO_4$ (a) x = 0.0, (b) x = 0.025, (c) x = 0.050, (d) x = 0.075, (e) x = 0.1 and (f) expanded view of the plane (311).

Table 1. Rietveld refined parameters of $Ni_{0.35}Mn_{0.35}Zn_{0.3}Fe_{2-x}Ce_xO_4$.

‘x’	‘a’ (Å)	χ^2	R_P	R_{WP}	R_{Exp}
0.0	8.4105	1.05	10.8	11.7	15.14
0.025	8.4135	1.05	10.5	11.1	13.78
0.050	8.4142	1.07	10.2	11.5	14.59
0.075	8.4185	1.08	12.1	14.5	16.34
0.1	8.4193	1.21	12.5	15.8	16.45

X-ray density of the powdered samples was calculated using the relation given in the literature [29], and the bulk density of the samples can be obtained using the relation $d_{Bulk} = M/\left(\pi r^2 h\right)$. It can be seen that the X-ray density increases from 5.2491 to 5.3401 gm/cc (Figure 2 (a). Percentage porosity of the samples was estimated by using the following relation [28]:

$$P(\%) = \left(\frac{d_X - d_{Bulk}}{d_X}\right) \times 100 \qquad (1)$$

Figure 2 (a) indicates that the porous nature of the sample decreases with the increasing percentage of Ce^{3+} ions in Ni-Mn-Zn ferrites. Crystallite size of the powdered samples was estimated by using the peak position (θ_B) and peak width (β_{FWHM}) of the most intensive peak (311) in the following relation [30];

$$t_{311} = \frac{K\lambda}{\beta_{FWHM} \mathrm{Cos}\theta_B} \qquad (2)$$

where K is crystallographic constant (K~0.9), λ-is the incident wavelength (1.5406 Å). From Figure 2 (b), it can be seen that the crystallite size of the samples increases from 21.73 to 22.71 nm with the addition of Ce^{3+} ions in Ni-Mn-Zn nanocrystals. The specific surface area ‘S’ for all the compositions was evaluated by using the following relation [29]:

$$S = \frac{6000}{t_{311} \times d_{Bulk}} \qquad (3)$$

Figure 2 (b) clearly shows that the introduction of Ce^{3+} ions decreases the specific surface area ‘S’ from 62.18 to 56.91 m^2 gm^{-1}.

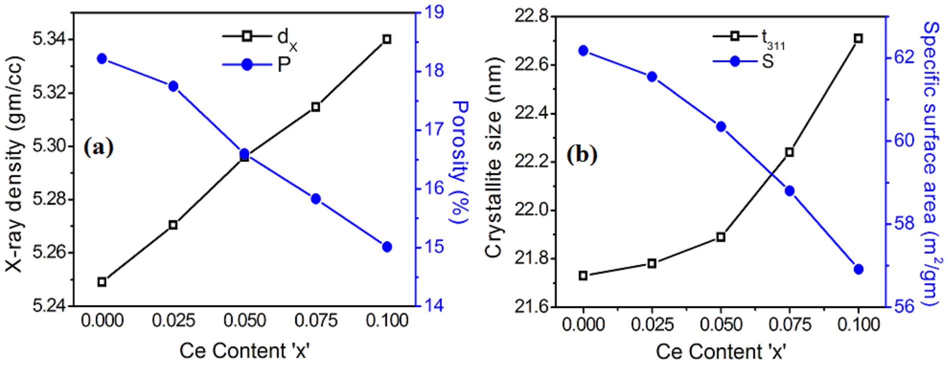

Figure 2. (a) variation of X-ray density (d_X) and porosity (P), (b) variation of crystallite size (t_{311}) and specific surface area (S) with Ce^{3+} content ‘x’ in $Ni_{0.35}Mn_{0.35}Zn_{0.3}Fe_{2-x}Ce_xO_4$.

The shape size and morphology of the sample were studied by using scanning electron microscopy images. Figure 3 (a, b, and c) shows the SEM images of the samples x = 0.0, 0.05 and 0.1, respectively. SEM images indicate that most of the grains have an approximately spherical shape with some agglomeration. The average grain size was estimated using the software Image J, and the grain size distribution is shown in histograms of Figure 3 (d, e, and f). Similar to crystallite size, grain size also increases from 30 nm to 33 nm, substituting Ce^{3+}

ions in Ni-Mn-Zn ferrites. Figure 4 (a, b and c) respectively shows the EDAX spectra of typical samples x = 0.0, 0.05 and 0.1. The table shown in Figure 4 (d) gives the atomic and weight percentage of constituent elements, which almost agrees with the prepared stoichiometric proportion. Analysis of EDAX spectra confirms that all the expected constituent elements are present in the ferrites without any impurity.

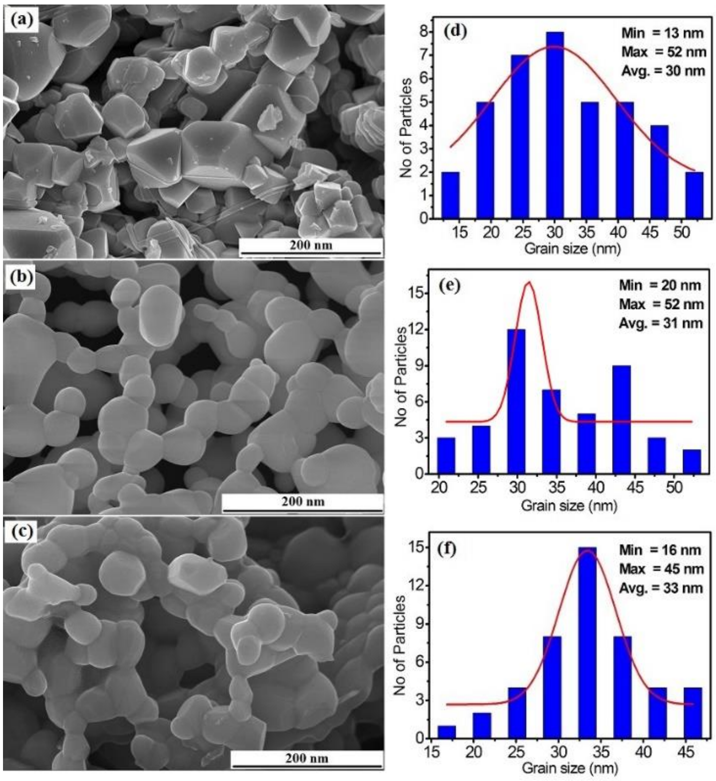

Figure 3. Scanning electron micrographs of the samples (a) x = 0.0, (b) x = 0.05, (c) x = 0.1; and histograms of (d) x = 0.0, (e) x = 0.5, (f) x = 0.1 for $Ni_{0.35}Mn_{0.35}Zn_{0.3}Fe_{2-x}Ce_xO_4$.

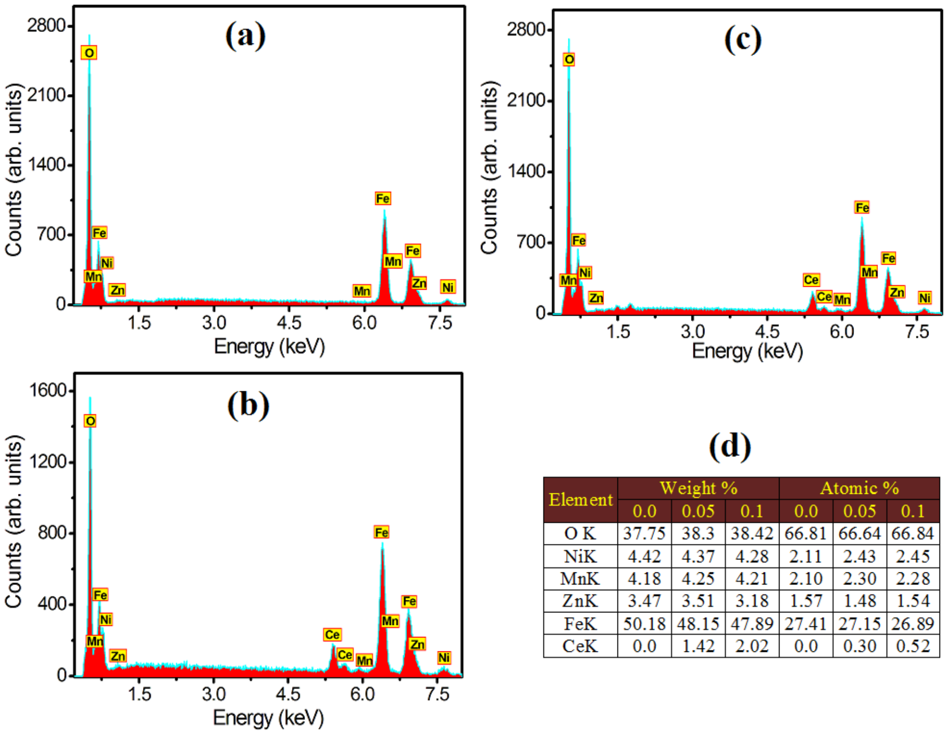

Element	Weight %			Atomic %		
	0.0	0.05	0.1	0.0	0.05	0.1
O K	37.75	38.3	38.42	66.81	66.64	66.84
NiK	4.42	4.37	4.28	2.11	2.43	2.45
MnK	4.18	4.25	4.21	2.10	2.30	2.28
ZnK	3.47	3.51	3.18	1.57	1.48	1.54
FeK	50.18	48.15	47.89	27.41	27.15	26.89
CeK	0.0	1.42	2.02	0.0	0.30	0.52

Figure 4. Energy dispersive X-ray analysis spectra of $Ni_{0.35}Mn_{0.35}Zn_{0.3}Fe_{2-x}Ce_xO_4$ where (a) x = 0.0, (b) x = 0.05, (c) x = 0.1 and (d) weight and atomic percentage of constituent elements.

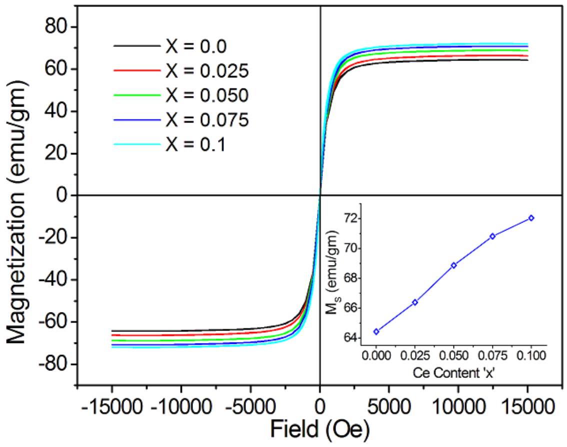

Figure 5. Hysteresis curves of $Ni_{0.35}Mn_{0.35}Zn_{0.3}Fe_{2-x}Ce_xO_4$ (inset shows the variation of saturation magnetization with Ce^{3+} substitution).

The magnetic behavior of Ce^{3+} substituted Ni-Mn-Zn soft ferrites sintered at 900^0C is illustrated in Figure 5. Replacement of Fe^{3+} ions by Ce^{3+} ions in Ni-Mn-Zn crystal lattice at octahedral – B site increases the saturation magnetization (M_s) linearly. The inset of Figure 4 shows that saturation magnetization (M_s) increases from 64.42 to 72.04 emu/gm. Bohr magneton number 'n_B' (μ_B) was computed using the following relation [31]:

$$n_B(\mu_B) = \frac{M_W \times M_S}{N_A \times 9.27 \times 10^{-21}} \qquad (4)$$

where, M_w is the molecular weight of the sample, M_s is saturation magnetization, and N_A is Avogadro's number. Computed values of Bohr magneton (n_B) show an increasing trend from 2.71 to 3.09 (μ_B) with the substitution of Ce^{3+} ions in Ni-Mn-Zn spinel ferrites.

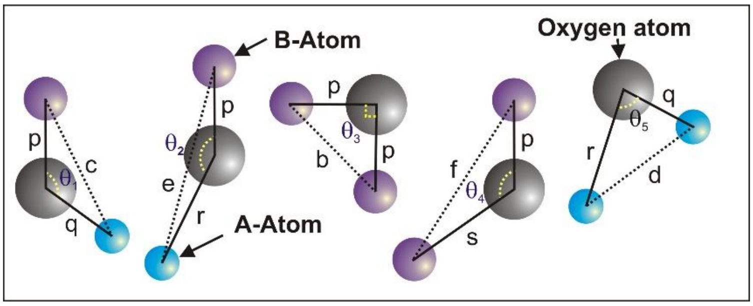

Figure 6. Favorable ion-pair configurations with interionic distances (M_e-O, and M_e-M_e) and bond angles (θ).

In general, the magnetic behavior of spinel ferrites is strongly dependent on the three common magnetic interactions. Super exchange mechanism produces such interactions (A-A, A-B, and B-B) among the cations and neighboring anions in spinel ferrites. The strength of these interactions is completely susceptible to the bond lengths (M_e-O and M_e-M_e) and bond angles (θ). As strength is inversely proportional to bond lengths, A-B interactions are stronger than A-A and B-B interactions due to their shorter bond lengths. Figure 6 illustrates the favorable ion-pair configurations with inter-ionic distances and bond angles. Cation - anion distances (p, q, r, and s), cation-cation distances (b, c, d, e, and f) and bond angels (θ_1, θ_2, θ_3, θ_4, and θ_5) were computed by using the equations given in Table 2 with their computed values for each composition [10, 32]. It can be seen that both cations – anion (M_e-O) and cation – cation (M_e-M_e) distances increased with the substitution of Ce^{3+} ions in Ni-Mn-Zn ferrites. These results are analogs with the increase in lattice parameter, which increases the unit cell volume [32]. Bond angles associated with the A-B interactions (θ_1 and θ_2) and A-A interaction

(θ_5) are found to be decreased with Ce^{3+} substation, suggesting the weakening of A-B and A-A interactions in Ni-Mn-Zn ferrites. While as increasing bond angles (θ_3 and θ_4) suggesting the strengthening of B-B interactions with the substitution of Ce^{3+} ions in Ni-Mn-Zn spinel lattice.

Table 2. Interionic distances (M_e-O, M_e-M_e) and bond angles (θ) of $Ni_{0.35}Mn_{0.35}Zn_{0.3}Fe_{2-x}Ce_xO_4$.

↓Formula \ ‘x’→	**0.0**	**0.025**	**0.050**	**0.075**	**0.1**
M_e-O distances					
$p = a\left(\frac{5}{8} - u\right)$Å	1.9455	1.9459	1.9458	1.9464	1.9462
$q = a\sqrt{3}\left(u - \frac{1}{4}\right)$Å	2.2596	2.2693	2.2797	2.2890	2.2994
$r = a\sqrt{11}\left(u - \frac{1}{4}\right)$Å	4.3268	4.3453	4.3653	4.3831	4.4031
$s = a\sqrt{3}\left(\frac{u}{3} + \frac{1}{8}\right)$Å	3.8806	3.8895	3.8987	3.9075	3.9167
M_e- M_e distances					
$b = \sqrt{2}\left(\frac{a}{4}\right)$Å	3.0642	3.0698	3.0754	3.0810	3.0866
$c = \sqrt{11}\left(\frac{a}{8}\right)$Å	3.5931	3.5997	3.6062	3.6128	3.6194
$d = \sqrt{3}\left(\frac{a}{4}\right)$Å	3.7529	3.7598	3.7666	3.7734	3.7803
$e = \sqrt{3}\left(\frac{3a}{8}\right)$Å	5.6294	5.6396	5.6499	5.6602	5.6704
$f = \sqrt{6}\left(\frac{a}{4}\right)$Å	5.3074	5.3171	5.3268	5.3365	5.3461
Bond angles					
$\theta_1 = \cos^{-1}\left(\frac{p^2 + q^2 - c^2}{2pq}\right)$	117.27	117.15	117.02	116.91	116.78
$\theta_2 = \cos^{-1}\left(\frac{p^2 + r^2 - e^2}{2pr}\right)$	123.12	122.77	122.37	122.05	121.65
$\theta_3 = \cos^{-1}\left(\frac{2p^2 - b^2}{2p^2}\right)$	103.96	104.20	104.48	104.70	104.98
$\theta_4 = \cos^{-1}\left(\frac{p^2 + s^2 - f^2}{2ps}\right)$	128.20	128.24	128.29	128.33	128.38
$\theta_5 = \cos^{-1}\left(\frac{r^2 + q^2 - d^2}{2rq}\right)$	60.15	59.91	59.65	59.44	59.18

Dielectric constant (ε′) for all the samples was computed by using the relation $\varepsilon' = Cd/\varepsilon_0\pi r^2$, where C-is capacitance, d-is sample thickness, r-is radius of the disc-shaped sample, and ε_0- is the free space absolute permittivity. Plots are drawn between dielectric constant and applied frequency within the range of 50 Hz to 5 MHz. Figure 7 (a) shows the typical behavior of spinel ferrites which shows higher values of dielectric constants at low frequencies and decreases fast and becomes almost constant at high-frequency regions. This variation of the real part of permittivity can be explained based on atomic, electronic, ionic, and interfacial polarization [24]. The hopping mechanism suggests that, at the low-frequency region, hopping electrons cannot have sufficient energy to cross the highly resistive grain boundaries, which results in the formation of polarization at grain boundaries. According to Koop's phenomena and the Maxwell-Wagner model, ferromagnetic materials consist of two layers: highly conducting grains and highly resistive grain boundaries [33-36]. At the low-frequency region, the grain boundary effect is more predominant and hence shows a higher dielectric constant due to space charge polarization. At higher frequency regions, hopping electrons can easily cross the grain boundaries, and hence dielectric constant decreases sharply and becomes constant. Dielectric loss tangent (tan δ) is obtained by using the relation ($\tan\delta = \varepsilon'' / \varepsilon'$), and its variation is shown in Figure 7 (b). It is observed that the dielectric loss tangent follows similar behavior as seen for the dielectric constant. As described by Hudson [37], a material having high resistivity possesses low dielectric loss. Hence, Ce^{3+} doped Ni-Mn-Zn ferrites with low dielectric loss can be effectively used in high-frequency data storage applications.

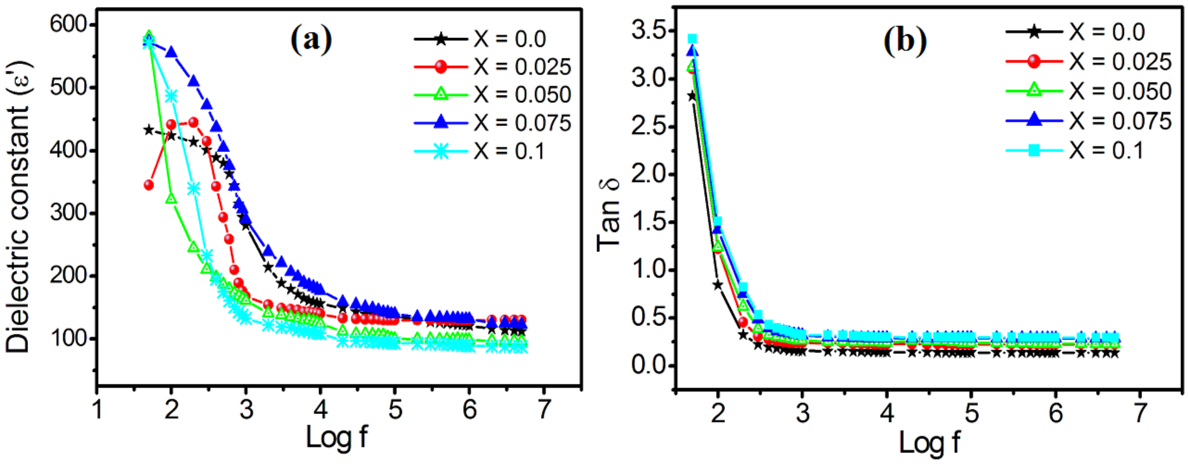

Figure 7.(a) Variation of dielectric constant (ε′) and (b) variation of dielectric loss tangent (tan δ) with log f for $Ni_{0.35}Mn_{0.35}Zn_{0.3}Fe_{2-x}Ce_xO_4$.

4. Conclusions

Ce^{3+} substituted Ni-Mn-Zn spinel ferrite nanoparticles with a chemical formula $Ni_{0.35}Mn_{0.35}Zn_{0.3}Fe_{2-x}Ce_xO_4$ was prepared by sol-gel auto-ignition process. The prepared samples possess a single-phase cubic spinel structure. Goodness factor ranging from 1.05 to 1.21 confirms the refinement quality of the X-ray patterns. Substitution of Ce^{3+} ions increases the lattice parameter, X-ray density, and crystallite size. SEM micrographs confirmed the spherical shape of the particles with some agglomeration, and the grain size obtained was in the range of 30 to 33 nm. EDAX spectra show the phase purity of the samples and observed atomic and weight percentages are in good agreement with their stoichiometric proportion in the compositions. Insertion of Ce^{3+} ions in Ni-Mn-Zn crystal lattice increases the saturation magnetization from 64.42 to 72.04 emu/g. Analysis of favorable ion-pair configurations suggesting the predominance of B-B interactions. Lower dielectric loss at higher frequency regions suggests that Ce^{3+} substituted Ni-Mn-Zn ferrites are suitable for high-frequency appliances.

Funding

This research received no external funding.

Acknowledgments

This research has no acknowledgment.

Conflicts of Interest

The authors declare no conflict of interest.

References

1. Rady, K.E.; Shams, M.S. Enhancement of structure, dielectric and magnetic properties of nanocrystalline Mn–Zn ferrites using Ni–Ti ions. *Journal of Materials Science: Materials in Electronics* **2020**, *31*, 22820-22832, https://doi.org/10.1007/s10854-020-04808-3
2. Nithiyanantham, S.; Viviliya, S.; Anadhan S.; Mahalakshmi, S. Synthesis and characterization of cobalt ferrite through Co-precipitation technique. *Lett. Appl. NanoBio.***2021,***10*, 1871-1876, https://doi.org/10.33263/LIANBS101.18711876.
3. Wadgane, S.R.; Alone, S.T.; Karim, A.; Vats, G.; Shirsath, S.E.; Kadam, R.H. Magnetic field induced polarization and magnetoelectric effect in Na0.5Bi0.5TiO3–Co0.75Zn0.25Cr0.2Fe1.8O4 multiferroic composite. *Journal of Magnetism and Magnetic Materials* **2019**, *471*, 388-393, https://doi.org/10.1016/j.jmmm.2018.10.011.
4. Kumar, Y.; Vashistha, V.K.; Das, D.K. Synthesis of pervoskite type $NdFeO_3$ nanoparticles and used as electrochemical sensor for detection of paracetamol. *Lett. Appl. NanoBio.***2020,***9*, 866-869, https://doi.org/10.33263/LIANBS91.866869.
5. Birajdar, A.A.; Shirsath, S.E.; Kadam, R.H.; Patange, S.M.; Mane, D.R.; Shitre, A.R. Rietveld structure refinement and cation distribution of Cr3+ substituted nanocrystalline Ni-Zn ferrites. *ISRN Ceramics* **2012,** *2012*, https://doi.org/10.5402/2012/876123.
6. Shirsath, S.E.; Kadam, R.H.; Mane, M.L.; Ghasemi, A.; Yasukawa, Y.; Liu, X.; Morisako, A. Permeability and magnetic interactions in Co2+ substituted Li0.5Fe2.5O4 alloys. *Journal of Alloys and Compounds* **2013**, *575*, 145-151, https://doi.org/10.1016/j.jallcom.2013.04.058.
7. Abu-Elsaad, N.I.; Mazen, S.A.; Nawara, A.S. Tertiary Ni0.7-xZn0.3MxFe2O4 (M=Mn, Co, and Cu) spinel ferrites: Electrical and dielectric properties. *Journal of Alloys and Compounds* **2021**, *856*, https://doi.org/10.1016/j.jallcom.2020.157794.
8. Saija, K.G.; Vasoya, N.H.; Modi, S.K.; Meshiya, U.M.; Jani, K.K.; Raval, P.Y.; Modi, K.B. Bulk magnetization, temperature - Dependent ac susceptibility and dc resistivity study on Mn0.7+xZn0.3SixFe2-2xO4 (x = 0.0–0.3) spinel ferrites. *Physica B: Condensed Matter* **2020**, *593*, https://doi.org/10.1016/j.physb.2020.412302.
9. Kadam, R.H.; Desai, K.; Shinde, V.S.; Hashim, M.; Shirsath, S.E. Influence of Gd3+ ion substitution on the MnCrFeO4 for their nanoparticle shape formation and magnetic properties. *Journal of Alloys and Compounds* **2016**, *657*, 487-494, https://doi.org/10.1016/j.jallcom.2015.10.164.
10. Kadam, R.H.; Borade, R.B.; Mane, M.L.; Mane, D.R.; Batoo, K.M.; Shirsath, S.E. Structural, mechanical, dielectric properties and magnetic interactions in Dy3+-substituted Co–Cu–Zn nanoferrites. *RSC Advances* **2020**, *10*, 27911-27922, https://doi.org/10.1039/D0RA05274D.
11. El-Shater, R.E.; El Shimy, H.; Assar, S.T. Investigation of physical properties of synthesized Zr doped Ni–Zn ferrites. *Materials Chemistry and Physics* **2020**, *247*, https://doi.org/10.1016/j.matchemphys.2020.122758.
12. Batoo K.M.; Kumar S.; Lee C.G. Influence of Al doping on electrical properties of Ni-Cd nano ferrites. *Current Appl. Phys.* **2009,** *9*, 826-832, https://doi.org/10.1016/j.cap.2008.08.001.
13. Ali, M.A.; Khan, M.N.I.; Hossain, M.M.; Chowdhury, F.U.Z.; Hossain, M.N.; Rashid, R.; Hakim, M.A.; Hoque, S.M.; Uddin, M.M. Mechanical behavior, enhanced dc resistivity, energy band gap and high temperature magnetic properties of Y-substituted Mg–Zn ferrites. *Materials Research Express* **2020**, *7*, https://doi.org/10.1088/2053-1591/ab7791.
14. Choudhari, S.S.; Shelke, S.B.; Batoo, K.M.; Adil, S.F.; Kadam, A.B.; Imran, A.; Hadi, M.; Raslan, E.H.; Shirsath, S.E.; Kadam, R.H. Mn0.7Zn0.3Fe2O4 + BaTiO3 composites: structural, morphological, magnetic, M–E effect and dielectric properties. *Journal of Materials Science: Materials in Electronics* **2021**, *32*, 10308-10319, https://doi.org/10.1007/s10854-021-05686-z.
15. Satpute, S.S.; Wadgane, S.R.; Kadam, S.R.; Mane, D.R.; Kadam, R.H. Y3+ substituted Sr-hexaferrites: sol-gel synthesis, structural, magnetic and electrical characterization. *Cerâmica* **2019**, *65*, 274-281, https://doi.org/10.1590/0366-69132019653742582.
16. Akhtar, P.; Akhtar, M.N.; Baqir, M.A.; Ahmad, A.; Khallidoon, M.U.; Farhan, M.; Khan, M.A. Structural and magnetic evaluations of rare-earths (Tb, Pr, Ce, Gd, Y)-doped spinel ferrites for high frequency and switching applications. *Journal of Materials Science: Materials in Electronics* **2021**, *32*, 7692-7703,https://doi.org/10.1007/s10854-021-05487-4.

17. Rezlescu, N.; Rezlescu, E.; Pasnicu, C.; Craus, M.L. Effects of the rare-earth ions on some properties of a nickel-zinc ferrite. *Journal of Physics: Condensed Matter* **1994**, *6*, 5707-5716,https://doi.org/10.1088/0953-8984/6/29/013.
18. Satpute, S.; Wadgane, S.; K. Desai; R. Mane, D.; Kadam, R. Substitution effect of Y3+ ions on the structural, magnetic and electrical properties of cobalt ferrite nanoparticles. *Cerâmica* **2020**, *66*, 43-49, https://doi.org/10.1590/0366-69132020663772734.
19. Rahimi-Nasrabadi, M.; Behpour, M.; Sobhani-Nasab, A.; Jeddy, M.R. Nanocrystalline Ce-doped copper ferrite: synthesis, characterization, and its photocatalyst application. *Journal of Materials Science: Materials in Electronics* **2016**, *27*, 11691-11697,https://doi.org/10.1007/s10854-016-5305-8.
20. Abdellatif, M.H.; Azab, A.A.; Salerno, M. Effect of rare earth doping on the vibrational spectra of spinel Mn-Cr ferrite. *Materials Research Bulletin* **2018**, *97*, 260-264, https://doi.org/10.1016/j.materresbull.2017.09.012.
21. Gadkari, A.B.; Shinde, T.J.; Vasambekar, P.N. Structural analysis of Y3+-doped Mg–Cd ferrites prepared by oxalate co-precipitation method. *Materials Chemistry and Physics* **2009**, *114*, 505-510, https://doi.org/10.1016/j.matchemphys.2008.11.011.
22. Gurav, S.K.; Shirsath, S.E.; Kadam, R.H.; Patange, S.M.; Lohar, K.S.; Mane, D.R. Less magnetic and larger Zr4+–Zn2+ ions co-substituted structural and magnetic properties of ordered Li0.5Fe2.5O4 nanoparticles. *Materials Research Bulletin* **2013**, *48*, 3530-3536,https://doi.org/10.1016/j.materresbull.2013.05.047.
23. Qamar, S.; Akhtar, M.N.; Aleem, W.; Rehman, Z.u.; Khan, A.H.; Ahmad, A.; Batoo, K.M.; Aamir, M. Graphene anchored Ce doped spinel ferrites for practical and technological applications. *Ceramics International* **2020**, *46*, 7081-7088,https://doi.org/10.1016/j.ceramint.2019.11.200.
24. Kamran, M.; Anis-ur-Rehman, M. Enhanced transport properties in Ce doped cobalt ferrites nanoparticles for resistive RAM applications. *Journal of Alloys and Compounds* **2020**, *822*, https://doi.org/10.1016/j.jallcom.2019.153583.
25. Shirsath, S.E.; Jadhav, S.S.; Toksha, B.G.; Patange, S.M.; Jadhav, K.M. Remarkable influence of Ce4+ ions on the electronic conduction of Ni1−2xCexFe2O4. *Scripta Materialia* **2011**, *64*, 773-776, https://doi.org/10.1016/j.scriptamat.2010.12.043.
26. Kadam, R.H.; Birajdar, A.P.; Alone, S.T.; Shirsath, S.E. Fabrication of Co0.5Ni0.5CrxFe2−xO4 materials via sol–gel method and their characterizations. *Journal of Magnetism and Magnetic Materials* **2013**, *327*, 167-171,https://doi.org/10.1016/j.jmmm.2012.09.059.
27. Desai, K.R.; Alone, S.T.; Wadgane, S.R.; Shirsath, S.E.; Batoo, K.M.; Imran, A.; Raslan, E.H.; Hadi, M.; Ijaz, M.F.; Kadam, R.H. X-ray diffraction based Williamson–Hall analysis and rietveld refinement for strain mechanism in Mg–Mn co-substituted CdFe2O4 nanoparticles. *Physica B: Condensed Matter* **2021**, *614*,https://doi.org/10.1016/j.physb.2021.413054.
28. Levy, D.; Pavese, A.; Hanfland, M. Phase transition of synthetic zinc ferrite spinel (ZnFe2O4) at high pressure, from synchrotron X-ray powder diffraction. *Physics and Chemistry of Minerals* **2000**, *27*, 638-644,https://doi.org/10.1007/s002690000117.
29. Kadam, R.H.; Biradar, A.R.; Mane, M.L.; Shirsath, S.E. Sol-gel auto-combustion synthesis of Li3xMnFe2−xO4 and their characterizations. *Journal of Applied Physics* **2012**, *112*,https://doi.org/10.1063/1.4746746.
30. Lohar, K.S.; Pachpinde, A.M.; Langade, M.M.; Kadam, R.H.; Shirsath, S.E. Self-propagating high temperature synthesis, structural morphology and magnetic interactions in rare earth Ho3+ doped CoFe2O4 nanoparticles. *Journal of Alloys and Compounds* **2014**, *604*, 204-210,https://doi.org/10.1016/j.jallcom.2014.03.141.
31. Akther Hossain, A.K.M.; Biswas, T.S.; Yanagida, T.; Tanaka, H.; Tabata, H.; Kawai, T. Investigation of structural and magnetic properties of polycrystalline Ni0.50Zn0.50−xMgxFe2O4 spinel ferrites. *Materials Chemistry and Physics* **2010**, *120*, 461-467,https://doi.org/10.1016/j.matchemphys.2009.11.040.
32. Lakhani, V.K.; Pathak, T.K.; Vasoya, N.H.; Modi, K.B. Structural parameters and X-ray Debye temperature determination study on copper-ferrite-aluminates. *Solid State Sciences* **2011**, *13*, 539-547, https://doi.org/10.1016/j.solidstatesciences.2010.12.023.
33. Deonikar, V.G.; Kulkarni, V.D.; Rathod, S.M.; Kim, H. Fabrication and characterizations of structurally engineered lanthanum substituted nickel-cobalt ferrites for the analysis of electric and dielectric properties. *Inorganic Chemistry Communications* **2020**, *119*, https://doi.org/10.1016/j.inoche.2020.108074.
34. Maxwell, J.C. *Electricity Magnetism*.Volume 1, Section 328, Oxford Uni. Press, Oxford, **1954**.
35. Yager, W.A. The Distribution of Relaxation Times in Typical Dielectrics. *Physics* **1936**, *7*, 434-450,https://doi.org/10.1063/1.1745355.
36. Koops, C.G. On the Dispersion of Resistivity and Dielectric Constant of Some Semiconductors at Audiofrequencies. *Physical Review* **1951**, *83*, 121-124,https://doi.org/10.1103/PhysRev.83.121.
37. Priya, A.S.; Geetha, D.; Kavitha, N. Evaluation of structural and dielectric properties of Al, Ce co-doped cobalt ferrites. *Materials Research Express* **2018**, *5*,https://doi.org/10.1088/2053-1591/aacd1e.